ACS central science

http://pubs.acs.org/journal/acscii

Research Article

Continuum Crystallization Model Derived from Pharmaceutical Crystallization Mechanisms

Yael Tsarfati,[‖] Idan Biran,[‖] Eduard Wiedenbeck, Lothar Houben, Helmut Cölfen,* and Boris Rybtchinski*

Cite This: *ACS Cent. Sci.* 2021, 7, 900−908

Read Online

ACCESS | Metrics & More | Article Recommendations | Supporting Information

ABSTRACT: The crystallization mechanisms of organic molecules in solution are not well-understood. The mechanistic scenarios where crystalline order evolves directly from the molecularly dissolved state ("classical") and from initially formed amorphous intermediates ("nonclassical") are suggested and debated. Here, we studied crystallization mechanisms of two widely used analgesics, ibuprofen (IbuH) and etoricoxib (ETO), using direct cryogenic transmission electron microscopy (cryo-TEM) imaging. In the IbuH case, parallel crystallization pathways involved diverse phases of high and low density, in which the instantaneous formation of final crystalline order was observed. ETO crystallization started from well-defined round-shaped amorphous intermediates that gradually evolved into crystals. This mechanistic diversity is rationalized by introducing a continuum crystallization paradigm: order evolution depends on ordering in the initially formed intermediates and efficiency of molecular rearrangements within them, and there is a continuum of states related to the initial order and rearrangement rates. This model provides a unified view of crystallization mechanisms, encompassing classical and nonclassical pictures.

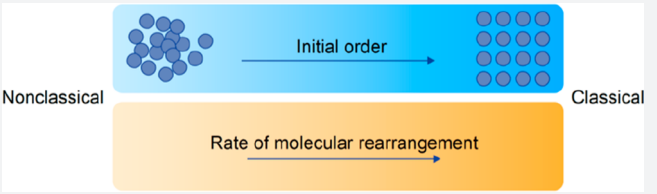

INTRODUCTION

Crystallization is important in biology,[1,2] geology,[3] materials science,[4−6] and industrial processes.[7] Crystallization in solution is central in many fields,[8−10] yet understanding its molecular mechanisms, especially at early stages, is limited, presenting a key challenge in chemistry.[11,12] Classical nucleation theory (CNT) implies the formation of nuclei whose structure is identical to that of the final crystalline phase. According to this view, nucleation involves dynamic and stochastic association of monomeric units (e.g., ions, atoms, or molecules) in a one-step process having a free-energy barrier at a critical nucleus size.[13−15] The nuclei then grow via monomer-by-monomer addition.[15] The observation of pathways involving various intermediate phases has challenged the classical nucleation picture.[12,16−19] Consequently, the "nonclassical nucleation" view was suggested, including the prenucleation cluster model[12,20] and the two-step nucleation theory.[15,21−23] This view implies that crystallization proceeds via an amorphous phase, in which nucleation takes place. However, "classical" and "nonclassical" views do not describe adequately the diversity and complexity of the observed crystallization mechanisms.[24,25]

Direct imaging of crystal evolution is essential for the development of mechanistic understanding. Crystallization of small organic molecules was studied by direct imaging only for a few systems.[26−31] The intrinsic difficulty to image organic systems is due to the small size of the solute species,[16] their often short lifetime, and their inherent sensitivity to the electron beam in the case of EM imaging.[32]

The majority of pharmaceutical products contains bioactive organic molecules in the crystalline solid state;[8] hence, obtaining insights into molecular drug crystallization is of great importance to the pharmaceutical industry.[33,9,34] Furthermore, control of pharmaceutical crystals' polymorphism represents a bottleneck in many late-stage drug development processes.[35] Insights into early stages of crystallization mechanisms of molecular pharmaceuticals in solution are difficult to obtain.[35,36] Mechanistic studies by AFM and spectroscopic methods[37−39] revealed complex processes of pharmaceutical crystallization, involving formation of amorphous intermediates[40] and attachment of supramolecular dimer units.[41] However, direct structural mapping of the entire nucleation/growth process of pharmaceutical molecular crystals has not been achieved. Imaging drug crystallization by *in situ* liquid cell TEM has been reported; however, it has inherent limitations (nucleation by electron beam, low resolution, and radiolysis), complicating reliable elucidation of crystallization mechanisms.[42,43] Time-resolved cryo-EM using low electron doses[44,45] was employed for imaging crystallization paths of organic dyes (perylene diimides, PDIs),[26,28,46] and proteins.[47,48] This methodology

Received: February 24, 2021
Published: April 23, 2021

https://doi.org/10.1021/acscentsci.1c00254
ACS Cent. Sci. 2021, 7, 900−908

proved to be adequate for imaging sensitive matter in solution (as vitrified samples).[49] While cryo-STEM is advantageous for thicker vitrified (biological) samples,[47] a more mature technique, cryo-TEM, enables imaging organic structures in solution with higher resolutions.[44,45,49]

Herein, we employed time-resolved cryo-TEM imaging to investigate entire crystallization paths of two widely used analgesics: ibuprofen (IbuH, Figure 1a),[40] and etoricoxib (ETO, Figure 1b).[50] In the case of IbuH, diverse aggregates that promoted *parallel crystallization paths* were observed, and crystalline order evolved fast and without initial densification, while in the case of ETO, order evolution from initially formed uniform aggregates was more gradual. Based on this mechanistic picture, we put forward a continuum crystallization model, implying that order evolution depends on the degree of ordering in the initially formed intermediates and efficiency of molecular rearrangements within them, spanning a continuum (from high to low) of order and rate.

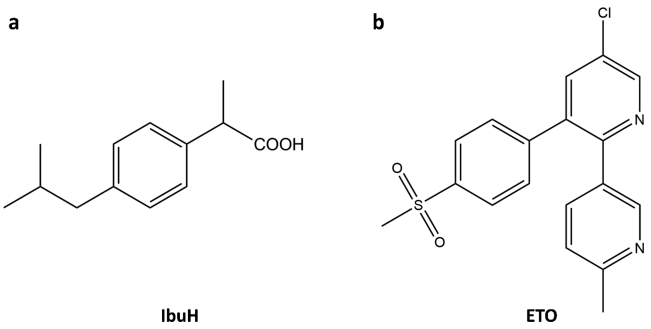

Figure 1. Molecular structures of (a) ibuprofen, IbuH; and (b) etoricoxib, ETO.

RESULTS AND DISCUSSION

Our choice of pharmaceutical molecules for crystallization studies was based on their broad medicinal use and specifics of their structure. IbuH is a small molecule with a single aromatic ring (Figure 1a), representing a limiting case in terms of contrast for TEM imaging. Spectroscopic studies on IbuH crystallization indicated involvement of amorphous precursors and allowed an insight into phase equilibrium (binodal and spinodal transitions); however, insights into morphology and structural details of the precursors were not available.[40] ETO has several directly connected aromatic rings and a more rigid 3D structure than IbuH, as well as two heteroatoms (S and Cl, Figure 1b), thus enabling elemental imaging using energy-dispersive X-ray spectroscopy (EDS).

Although the *S*-ibuprofen enantiomer is the active pharmaceutical ingredient (API),[51] *R*-ibuprofen is converted into the *S* enantiomer *in vivo*.[51] Thus, racemic ibuprofen is normally used in marketed formulations.[52] The carboxylic group of ibuprofen provides control over its water solubility via pH variation. Accordingly, we crystallized racemic ibuprofen using acidic titration.[40] Crystallization of IbuH in water was performed by titration of sodium ibuprofen salt (IbuNa) in aqueous solution with HCl (see the Experimental Section and Figure S1). The reaction mixture started as a clear solution of IbuNa that became turbid as the IbuH concentration was gradually increased. The crystallization process was studied by cryo-TEM imaging that captured structures relevant to IbuH order development (Figures 2 and 3) during the course of the stepwise titration (see the Experimental Section). The final precipitate had a structure that corresponded to that of a known crystalline form of IbuH[53] as evidenced by powder X-ray diffraction (pXRD, Figure S2) and electron diffraction (Figure 3l,m and Figure S3). Turbidity occurring at advanced titration stages (above 2 mL of HCl) indicated the formation of micron-size structures that are difficult to observe by cryo-TEM. However, order evolution was detected already in smaller structures. Moreover, imaging blotless samples that allow the observation of larger structures (see the Supporting Information for details) was consistent with the picture obtained by cryo-TEM imaging throughout the titration process.

Both low-density (Figure 2, Figure S4) and higher-density (Figure 3) IbuH intermediates formed at various titration volumes; the round-shaped morphology that is predominant for these aggregates may indicate microphase separation.[54] Some round low-density structures (368 ± 11 nm in diameter, 29 structures) were diffuse, having no well-defined boundary with the solution (Figure 2a,b and Figure S5−S7), whereas others had somewhat more defined boundaries (Figure 2e,f,h,j and Figure S8). The latter exhibited a significant variation in size, which can be grouped into structures having sizes of 62 ± 11 nm (8 structures) and 262 ± 67 nm (12 structures), with an overall diameter being 182 ± 113 nm; in blotless samples, similar larger structures were observed (diameters of 426 ± 215 nm, 8 structures). Notably, crystallinity was observed in a number of these structures. Thus, the diffuse intermediate displayed in Figure 2b exhibited a crystalline area (Figure 2c), whose FFT (Figure 2d) revealed spacing of 1.6 nm, which is typical of the ibuprofen crystal. Low-density round-shaped aggregates having partial order (Figure 2e−g, Figure S4) and crystalline domains (Figure 2h,i and Figure S9) with 1.6 nm spacing were also observed. An additional round-shaped aggregate having low density displayed crystallinity over its entire area (Figure 2j−m and Figures S10 and S11). The formation of crystalline domains that are ca. 10 nm in size (Figures S10 and S11) indicates uniform nucleation within the aggregates. In all low-density structures, crystalline order corresponds to the one of the IbuH crystals. It did not evolve gradually and was not concurrent with densification. This is distinctly different from gradual order evolution and densification previously observed by us in PDI crystallization.[28] We note that the instant formation of final crystalline order indicates the "classical mechanism", while its association with round-shaped aggregates is "nonclassical", pointing at a deficiency of such a dichotomy.

Cryo-TEM imaging also revealed denser structures, with and without crystalline order (Figure 3 and Figures S12−S17). They displayed several levels of densities, as indicated by higher-contrast regions and a lighter-contrast cloudlike material (Figure 3a,d). A significant number of denser aggregates, 171 ± 105 nm in size (43 structures) exhibited crystallinity. The spacings were found to be almost identical to those of the final crystals, according to the scanning transmission electron diffraction (STED, Figure 3l,m and Figure S18; see the Supporting Information for details) and FFT (see Figures 2−3 and Figures S14−S17 and S19). This indicates that the single IbuH crystalline form evolved in all intermediates. The final product of the process was identified as the one having the structure of a reported crystalline form of ibuprofen (Figure S20).[53,55]

Crystallization of ETO (Figure 1b) was induced by a direct addition of a methanol (MeOH) solution of ETO into water, resulting in 3.48×10^{-3} M water:MeOH = 9:1 (v/v) solution. The solution was transparent, and white needlelike crystals

https://doi.org/10.1021/acscentsci.1c00254
ACS Cent. Sci. 2021, 7, 900−908

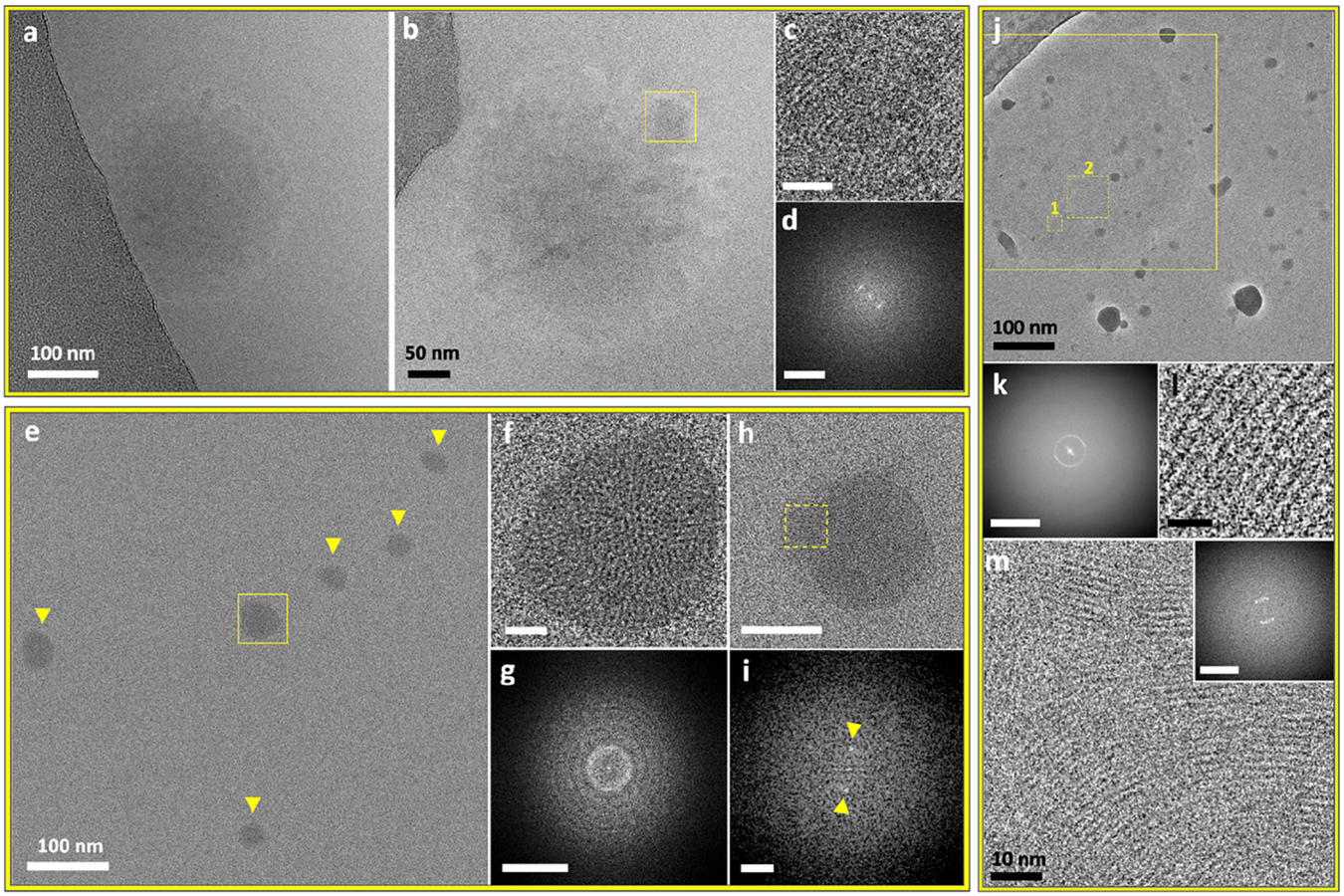

Figure 2. Cryo-TEM images of low-density intermediate phases in IbuH crystallization (resulting from IbuNa titration with HCl in aqueous medium). (a) Diffuse amorphous phase following titration with 2.2 mL of HCl. (b) Diffuse phase with a crystalline area, marked by the yellow square, following titration with 2.2 mL of HCl. (c) Magnified view of the marked area in part b displaying lattice fringes. Scale bar is 10 nm. (d) FFT of part c showing a *d*-spacing of 1.59 nm; scale bar is 2 nm^{-1}. (e) Area with several intermediates marked by arrows and a yellow square. (f) Magnified view of the aggregate marked in part e. Scale bar is 10 nm. (g) FFT of part f. Scale bar is 2 nm^{-1}. A bright distinct ring is apparent in part g (while absent in the FFT of the background, see Figure S8). The ring indicates randomly oriented crystalline domains with a 1.63 nm spacing. (h)Intermediate similar by morphology to those displayed in part e, exhibiting a crystalline domain, marked by the yellow square. Scale bar is 50 nm. (i) FFT of the region marked in part h, displaying FFT peaks (spots marked by arrows), corresponding to a *d*-spacing of 1.61. Scale bar is 1 nm^{-1}. (j) Extensive polycrystalline phase, following titration with 6 mL of HCl, imaged using a Volta phase plate. The background contains high-contrast ice contamination. (k) FFT of the marked area in part j that contains the intermediate phase (the largest square), showing a *d*-spacing of 1.6 nm. Scale bar is 2 nm^{-1}. (l) Representative image of a magnified crystalline area in part j (square 1), exhibiting lattice fringes with 1.55 nm spacing. Scale bar is 5 nm. (m) Representative image of a magnified crystalline area with multiple orientations in the intermediate in part j, corresponding to square 2. Inset: FFT of part m displaying a *d*-spacing of 1.61 nm. Scale bar is 2 nm^{-1}. The sharpness and contrast of the background in parts e, f, and h were adjusted to better distinguish the aggregates. The original images are presented in Figure S4.

precipitated within 1.5−2 h (Figure S21). These crystals corresponded to the known ETO crystalline form, as indicated by their pXRD (Figure S22).[56] ETO crystallization was studied by cryo-TEM imaging (Figures 4 and 5). At the early stages, up to 45 min of aging, amorphous round-shaped structures were observed (Figure 4a−f). The round aggregates were 320 ± 154 nm in diameter (75 structures) and were also observed by SEM imaging (diameter of 492 ± 149 nm, 80 structures, Figure 4a). Occasionally, structures with denser cores and a lighter-contrast external part were observed (Figure 4b−d,f). We confirmed that the spheres were composed of ETO, as evidenced by Cl and S peaks in the EDS spectrum (Figure S23). The spheres were detected in both blotted and blotless samples (Figure 4b−f and Figure S24a, respectively), supporting their significant population in the early stages of the process.

Following 25−45 min of aging (Figure 4g−m), some round structures exhibited crystallinity; e.g., the one presented in Figure 4g had a crystalline domain (Figure 4h). The aggregate presented in Figure 4j exhibited lattice fringes in the whole structure. A denser phase with an overall globular morphology having a core that is denser than the outer part was also observed (Figure 4k). In these structures, the spacings correspond to the ones in the known ETO crystal (Figure 4g−m and Figure S24d,e).[56]

Next, after 90 min of aging, larger higher-contrast structures were observed (Figure 5a−f). They were 1100 ± 565 nm in length and 763 ± 310 nm in width (13 structures), displaying a partially faceted morphology. Variation in the densities of different regions (Figure 5a,b,d,e and Figure S25) and rodlike areas within these structures were also observed (Figure 5b,e). These structures showed spacings corresponding to those found in ETO crystals.

After 2 h of aging, rodlike 1 μm long crystals (Figure 5g−m) and millimeter-long crystalline structures were observed at the bottom of the crystallizing solution (Figures S21 and S26a). EDS measurements confirmed that the crystals are composed of

https://doi.org/10.1021/acscentsci.1c00254
ACS Cent. Sci. 2021, 7, 900−908

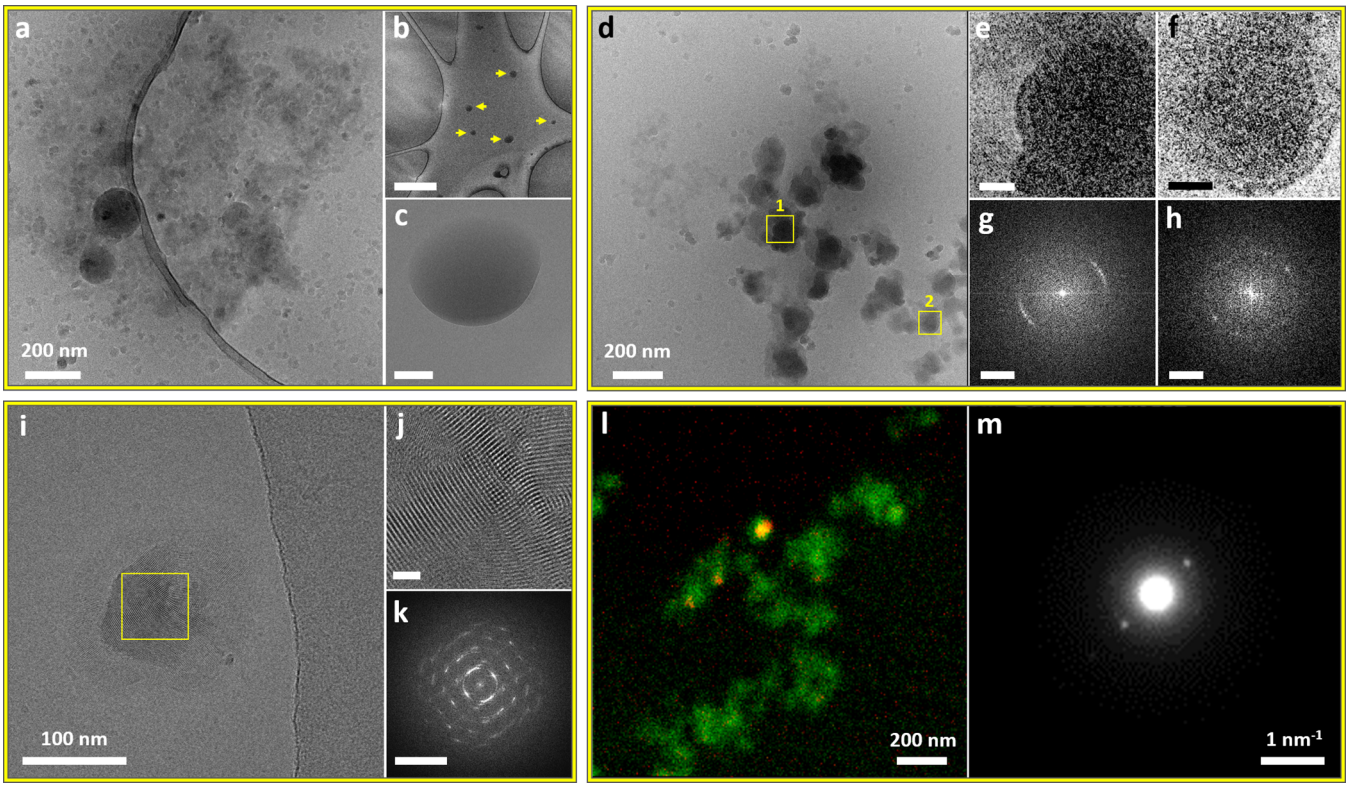

Figure 3. Cryo-TEM images of intermediate phases in IbuH crystallization, resulting from IbuNa titration with HCl in an aqueous medium. (a–c) Titration with 3 mL of HCl: (a) Spherical aggregates embedded in a cloudlike material. The background contains ice contamination. A low-magnification image of part a is presented in Figure S12. (b, c) Blotless samples. (b) Low-magnification image of several amorphous phases (marked by yellow arrows). Scale bar is 2 μm. (c) Magnified view of a representative aggregate shown in part b. Scale bar is 100 nm. (d) Dense aggregates following titration with 2.4 mL of HCl. (e, f) Magnified views of the areas marked by squares 1 and 2 in part d, exhibiting lattice fringes. Scale bars are 20 nm. (g, h) FFTs of parts e and f, respectively, showing a *d*-spacing of 1.57 nm. Scale bars are 0.5 nm^{-1}. (i) Crystalline intermediate (titration with 1 mL of HCl). (j) Magnified view of the marked area in part i. Lattice fringes are apparent. Scale bar is 10 nm. (k) FFTs of part j displaying *d*-spacings from 1.57 nm down to 0.43 nm. Scale bar is 2 nm^{-1}. (l, m) STED measurement, scanning an area with a cluster of underdeveloped dense nanocrystals (by a morphology similar to the aggregates displayed in parts d and i) following titration with 6 mL of HCl: (l) Color mix image of the scanned area with the HAADF signal in green, overlaid with the location of electron diffraction originating from crystalline diffraction around a *d*-spacing of 1.6 nm in red. (m) Averaged diffraction pattern derived from all diffraction patterns showing high correlation with 2-fold symmetry in the scanned area.

ETO (Figure S26b). The structure of crystalline intermediates and the crystalline product corresponded well to the reported crystal structure, as indicated by *d*-spacings observed in FFT, STEM imaging, and pXRD measurements (Figure 5l,m and Figure S22).

The crystallization mechanisms of IbuH and ETO exhibit several significant differences (Figure 6a). The most striking feature of the IbuH system is the diversity of initially formed structures and crystallization observed in them. In the case of ETO, only round-shaped structures of one type are observed (Figure 4a–f). The formation of diverse IbuH structures can be associated with crystallization conditions, upon which the acidic titration leads to a high concentration of strongly interacting hydrophobic moieties capable of multiple interaction modes. The appearance of crystalline order in both the low-density diffuse structures (Figure 2) and in the dense ones (Figure 3) suggests that a variety of initially formed phases are partially crystalline or evolve order quickly and exhibit parallel crystallization pathways originating from different prenucleation aggregates.[11,57] While suggested for inorganic systems,[11,57] it has not been observed in organic crystallization. Based on our observations, we propose here a general outlook on the organic crystallization mechanisms in solution, unifying and expanding the current classical and nonclassical views (Figure 6b). First, the individual molecules (present in the initial molecular solutions) partially desolvate and interact to form aggregates and newly nucleated phases of varying density and order. The dynamics of their formation as well as their structure define whether the observed pathway is close to "classical", where crystals are formed fast, or "nonclassical", where several intermediate structures are formed with slow dynamics, resulting in gradual order evolution (Figure 6b).

Depending on the conditions and molecular structure, the initial aggregation may bring about phases with different degrees of ordering: it may result in order that is close to crystalline ("classical mechanism") as in IbuH, or more distant from it (as in the ETO case). In addition, the varying ability of molecules in the aggregates to rearrange toward crystalline order may result in faster or slower dynamics of order evolution, so that the initial ordering and the speed of molecular rearrangements define the type of the crystallization process. Conceivably, there is a continuous spectrum of order in the initially formed aggregates, from a highly disordered amorphous to crystalline one, and varying rates of ordering, depending on molecular structure and crystallization conditions. We call this view a "continuum crystallization" model, which is inclusive of classical and nonclassical scenarios (Figure 6b).

https://doi.org/10.1021/acscentsci.1c00254
ACS Cent. Sci. 2021, 7, 900–908

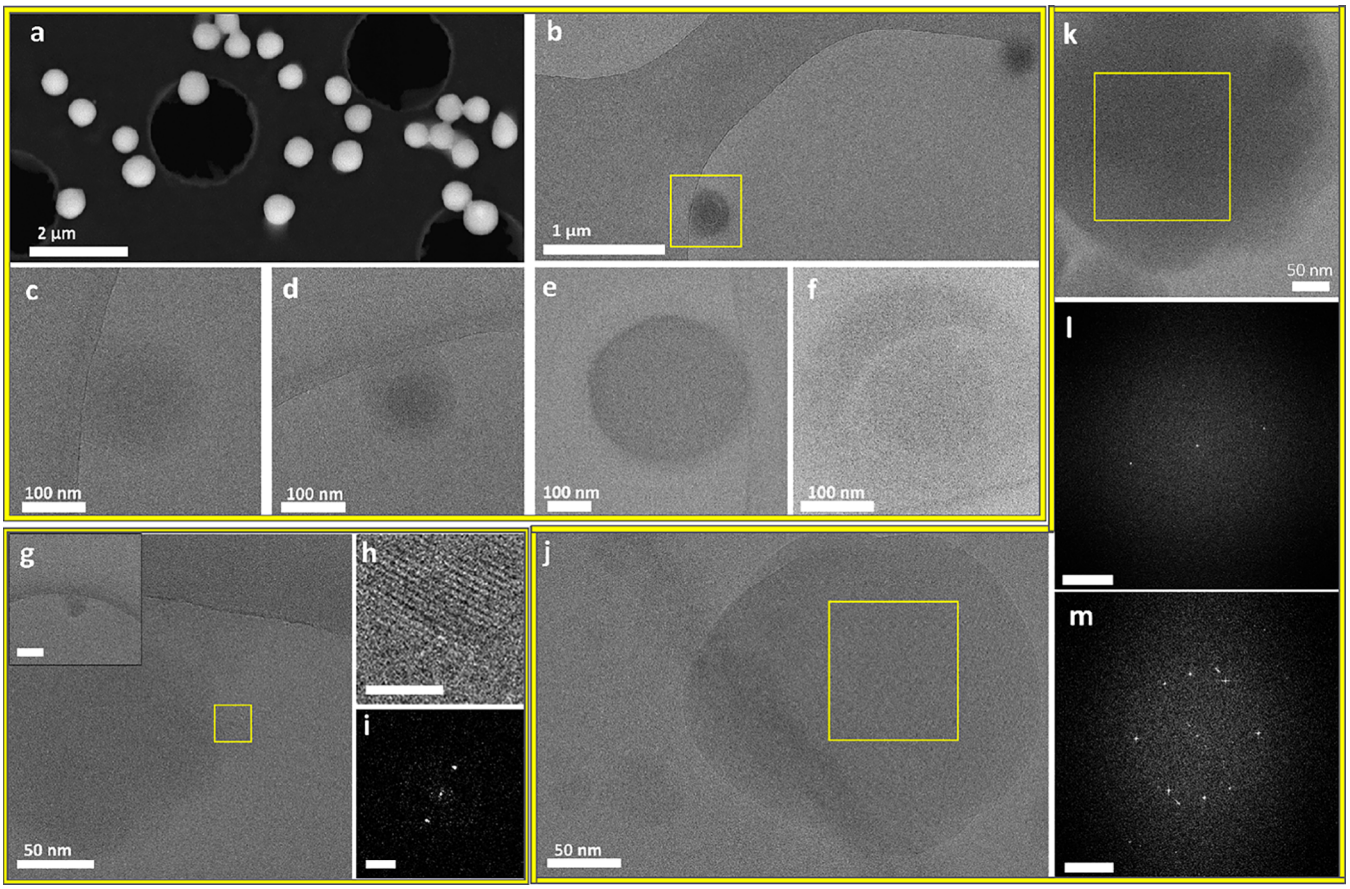

Figure 4. Amorphous ETO phases after 1 min (a), 3 min (c, d), and 15 min (b, e, f) following initial mixing (3.48×10^{-3} M ETO in water:MeOH = 9:1 (v/v) solution): (a) Representative SEM image of a dried sample. (b) Cryo-TEM image of an area containing two round amorphous aggregates. (c, d) Cryo-TEM images of diffuse round-shaped structures, showing a density gradient from the core to periphery. (e) Cryo-TEM image of an amorphous sphere displaying a uniform density and well-defined boundary. (f) Magnified view of the marked area in part b, showing a round aggregate with a denser core compared to its peripheral area. Cryo-TEM images of the crystallization intermediates after 45 min (g–i), 25 min (j), and 30 min (k–m) following initial mixing (3.48×10^{-3} M ETO in water:MeOH = 9:1 (v/v) solution): (g) Structure showing order in the peripheral area (marked in yellow). Inset: low-magnification view of part g. Scale bar is 200 nm. (h) Enlarged inverse FFT of part i, revealing the lattice fringes. Scale bar is 5 nm. (i) FFT of the marked area in part g, showing a *d*-spacing of 0.48 nm. Scale bar is 2 nm^{-1}. (j) Round structure with a sharp border with the solution. Fringes are visible in the majority of the aggregate. (k) Aggregate with varying density. (l) FFT of the marked area in part k displaying a *d*-spacing of 0.36 nm. Scale bar is 2 nm^{-1}. (m) FFT of the marked area in part j, displaying a *d*-spacing of 0.4, 0.36, and 0.98 nm, which correlate to the ones in the reported ETO crystal. Scale bar is 2 nm^{-1}.

SUMMARY

Cryo-TEM imaging provided direct insights into the crystallization of two pharmaceutical molecules, IbuH and ETO. Our studies reveal the structural development during the entire paths of pharmaceutical crystallization; such information has not been available until now. IbuH crystallization does not comply with either classical or nonclassical views, exhibiting multiple crystallization modes and a particularly diverse space of crystallization intermediates. ETO crystallization starts from well-defined round-shaped intermediates and is slower and more gradual. We propose a "continuum crystallization" model that takes into account the spectrum of ordering in the initially formed intermediates and efficiency of molecular rearrangements within them, unifying the classical and nonclassical crystallization views. In addition, our continuum model extends the mechanistic picture suggested by classical and nonclassical theories, by a consideration that nucleation and growth are driven by the initial molecular interactions and the subsequent dynamics of their optimization. Consequently, the course of a crystallization pathway defines the crystallization outcome. Thus, there is a continuum of possible structural and temporal states leading to crystal nucleation and growth, including a possibility of multiple pathways leading to the different or identical crystalline phases.

Regarding the current understanding of crystallization, the classical crystallization theory has existed for many decades, while a theoretical description of the nonclassical model, including the prenucleation cluster pathways or two-step nucleation as well as particle-based crystallization including oriented attachment and mesocrystal formation, is yet to be finalized. Our results and those of others indicate that crystallization is more complex than anticipated by the classical and nonclassical crystallization scenarios.[25] The continuum paradigm broadens the view on crystallization and helps to explain crystallization mechanisms that so far have not been understood. The different intermediates, which we have detected for IbuH, also point out that many species can exist in a crystallization system, being critical to polymorph selection and ultimately to its control. The latter is one of the long-standing goals in the crystallization of pharmaceutical molecules.

https://doi.org/10.1021/acscentsci.1c00254
ACS Cent. Sci. 2021, 7, 900–908

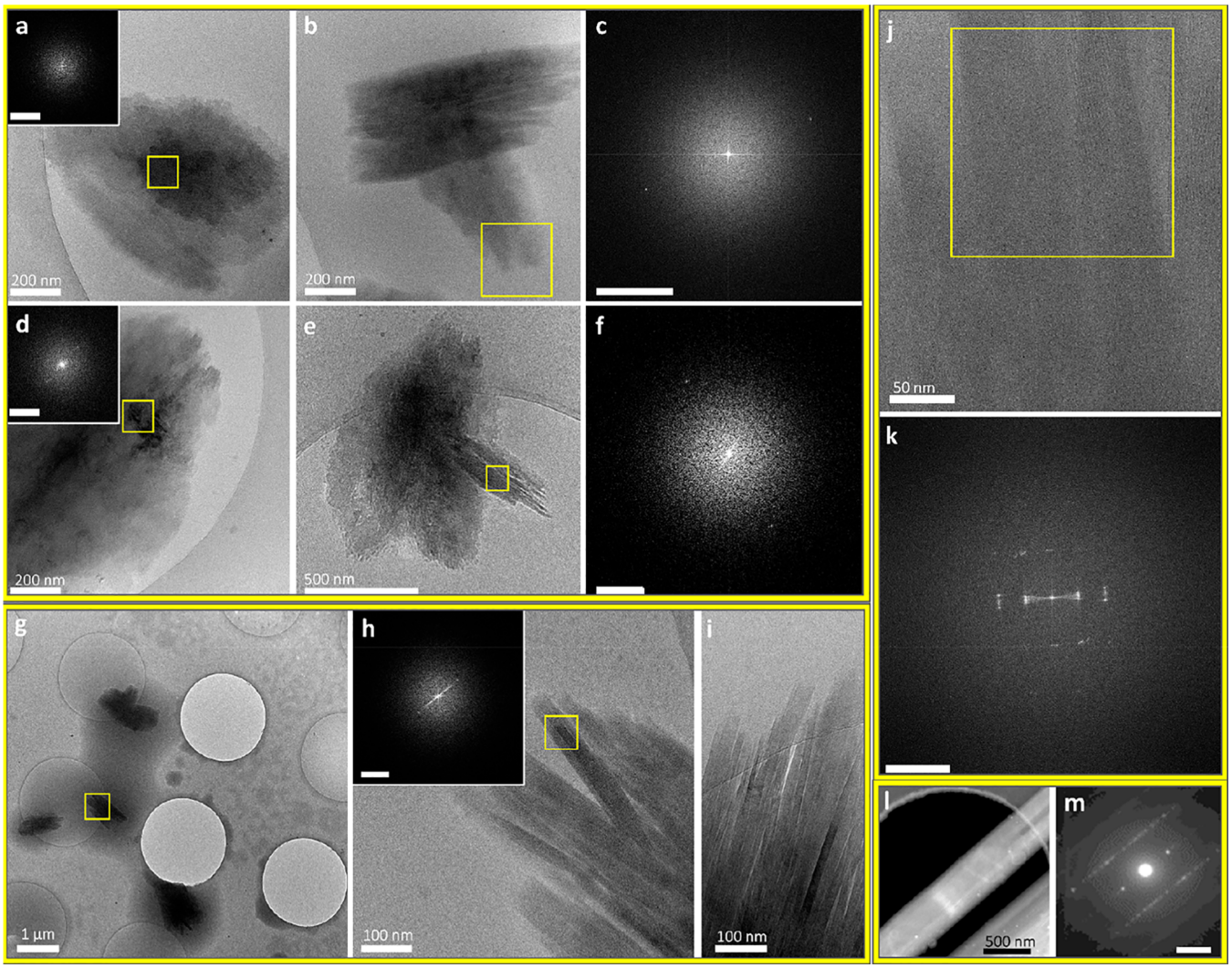

Figure 5. TEM and cryo-TEM images of (a–f) crystallization intermediates, 90 min aging, and (g–m) developed ETO needlelike crystals: (a) Sheetlike structure. Inset: FFT on the marked area displaying a *d*-spacing of 0.94 nm. Scale bar is 1 nm^{-1}. (b) High-contrast structure with partial faceting. (c) FFT on the marked area of part b, displaying a *d*-spacing of 0.86 nm. Scale bar is 1 nm^{-1}. (d) Large high-density structure. Inset: FFT on the marked area, displaying a *d*-spacing of 1.31 nm. Scale bar is 1 nm^{-1}. (e) Low-magnification image of needles emerging from the high-density structure. (f) FFT of the marked area of part e, displaying a *d*-spacing of 0.58 nm. Scale bar is 1 nm^{-1}. (g) High-contrast aggregates scattered on the grid. (h) Magnified view of the area marked in part g, showing bundles of needles. Inset: FFT of the marked area, revealing 1.14 nm spacing. Scale bar is 1 nm^{-1}. (i) High-magnification cryo-TEM image of needles. (j) High-magnification cryo-TEM image of needles with similar thicknesses. (k) FFT of the marked area in part j, displaying a *d*-spacing of 0.41 nm. Scale bar is 2 nm^{-1}. (l) Room-temperature dark-field STEM image of a needlelike crystal (from aged solution, drop-cast on a grid and dried overnight). (m) Averaged electron diffraction pattern of the thin areas found in part l. *d*-spacings derived from the diffraction pattern are 0.43 and 0.57 nm. Scale bar is 2 nm^{-1}.

EXPERIMENTAL SECTION

Cryo-(S)TEM. *Image Acquisition.* Imaging was performed at liquid nitrogen temperature on a Tecnai T12 instrument (Twin, Thermo Fisher Scientific) operating at 120 kV, Tecnai G2 F20 instrument (Twin, Thermo Fisher Scientific) operating at 200 kV, Talos Arctica G3 instrument (Thermo Fisher Scientific) operating at 200 kV, and on a Titan Krios G3i instrument (Thermo Fisher Scientific) operating at 300 kV. Specimens were introduced into the T12 and F20 microscopes using a Gatan 626 cooling holder and transfer station, or Autoloader for the Arctica and Titan instruments, and were equilibrated at −178 °C prior to imaging. Images were recorded using (1) a TVIPS F244HD CCD digital camera or Gatan OneView CMOS camera, on the Technai T12 instrument; (2) a Gatan US4000 CCD digital instrument; (3) a Gatan OneView CMOS camera on the Talos Arctica; and (4) a Falcon 3EC direct electron detector (Thermo Fisher Scientific), using the electron counting mode. A Volta phase plate was applied in specified cases on the Titan Krios instrument. Analysis and processing of the movies and images were done using Digital Micrograph, GMS 3, imageJ, and irfanview. The samples were imaged at various magnifications, using total electron doses not exceeding 20 $e/Å^2$.

Preparation of Standard Blotted Vitrified Samples. Samples were prepared by applying 6.5 μL of each sample to 300-mesh copper grids coated with holey carbon or 300-mesh Quantifoil R2/1 or R2/2 that were glow-discharged for 1 or 2 min prior to sample application. The samples were blotted for 2.5 s at 21 °C and 93–95% relative humidity and plunged into liquid ethane (after 1 s postblotting) using a Leica EM-GP automatic grid plunger or a Vitrobot Mark IV (FEI Company) plunging systems.

https://doi.org/10.1021/acscentsci.1c00254
ACS Cent. Sci. 2021, 7, 900–908

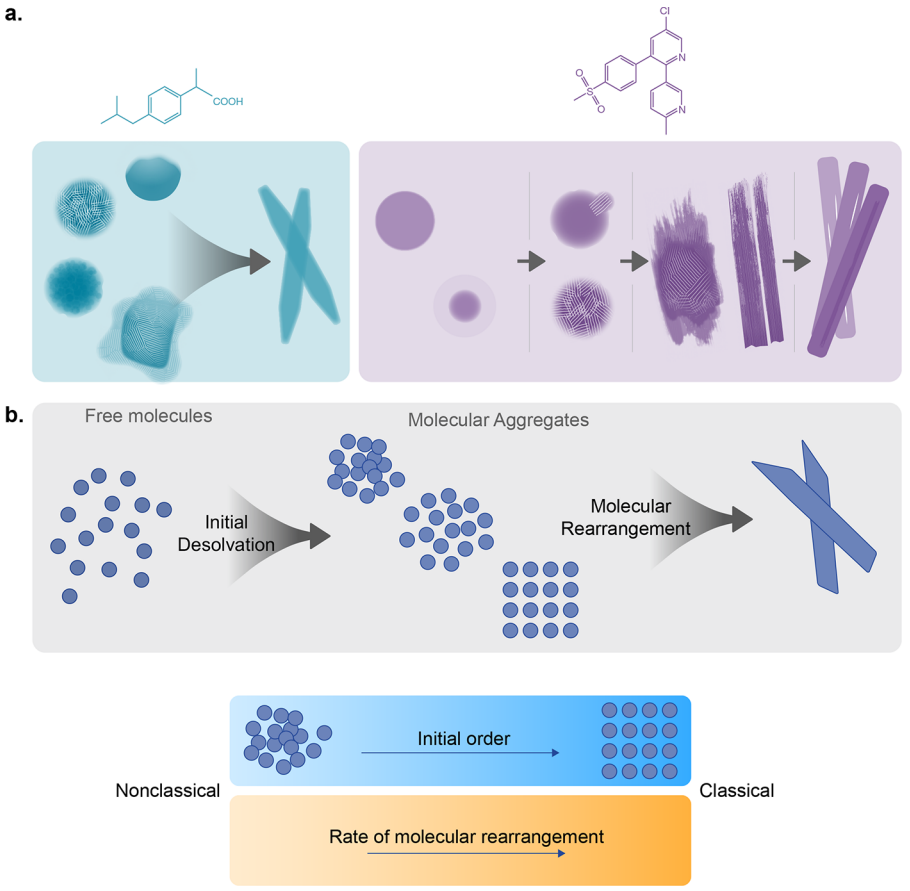

Figure 6. (a) Schematic of order evolution in IbuH and ETO crystallization. (b) Continuum crystallization model, where higher initial order and faster molecular rearrangements correspond to a "classical" end of the continuum.

Note that, unless stated otherwise, the default cryo-TEM sample is a standard blotted sample. The particle sizes were measured using Digital Micrograph, GMS 3, imageJ, and irfanview software. The related histograms are presented in Figures S27 and S28. Most samples were uniform as for the types of phases that were detected in them, and the same crystallization behavior was observed by TEM in different crystallization batches.

Preparation of Blotless Vitrified Samples. Samples were prepared by applying 30 nL of each sample to 300-mesh copper grids coated with double-layer holey carbon that was glow-discharged for 30 s. The samples were then immediately plunged into liquid ethane using a Leica EM-GP automatic grid plunger.

Scanning Transmission Electron Diffraction (STED). Vitrified samples were prepared similarly to those for the cryo-TEM imaging and introduced to the microscope using a high-tilt Gatan 914 cryotransfer tomography holder. Dried samples were prepared as those for TEM at room temperature (RT) and were also introduced using a Gatan 914 cryotransfer tomography holder at RT, then cooled under the microscope vacuum, and equilibrated at −178 °C prior to the imaging. Scanning transmission electron diffraction data were obtained using a double aberration-corrected Themis Z microscope (Thermo Fisher Scientific) equipped with a high-brightness FEG at an acceleration voltage of 200 kV. For the diffraction recording, an electron probe with a convergence angle of 0.2 mrad was adjusted in STEM microprobe mode and further defocused by typically 5−10 μm to reduce electron flux. The EMPAD (electron microscope pixel array detector)[58] allowed rapid data collection of the entire unsaturated diffraction pattern with a pixel dwell time of 1 ms for each pattern. EMPAD is a 128 × 128 pixel detector that consists of a 500 μm thick silicon diode bump bonded to a readout application specific integrated circuit. Each pixel has complete readout electronics consisting of an amplifier, discriminator, and counter. Thin-pixel circuitry provides a 1 000 000:1 dynamic range within a single frame, allowing the direct electron beam to be imaged while still maintaining single electron sensitivity. Analysis of the 4D STED data stacks was done using custom-written software.

EDS. For the Technai F20 microscope, EDS spectra and elemental maps were obtained with an EDAX Genesis (EDAX Inc., Mahwah, NJ) liquid N_2 cooled Si(Li) detector in STEM microprobe mode.

For the Titan Themis microscope, EDS hyperspectral data were obtained with a Super-X G2 four-segment SDD detector with a probe semiconvergence angle of 0.2 mrad and a beam current of approximately 30 pA.

SEM. SEM images were obtained using a Zeiss Gemini SEM 500 instrument:

(1) in transmission mode using a STEM detector in dark field mode (imaging and EDS were performed at a landing voltage of 30 kV with a 30 μm aperture);

(2) using the low vacuum secondary electron detector (LVSE) under a bias of 300 V and chamber pressure of 47 Pa [imaging was performed at a landing voltage of 5 kV with a 20 μm aperture in high current mode using analytical gun mode, and EDS data were collected using a Bruker SDD detector (XFlash 6)].

https://doi.org/10.1021/acscentsci.1c00254
ACS Cent. Sci. 2021, 7, 900−908

The SEM images of the matured crystals were obtained using a Zeiss Ultra 55 instrument. Imaging and EDS were acquired at a landing voltage of 15 kV with a 30 mm aperture. EDS data were collected using a Bruker 60 mm SDD detector (XFlash 6).

Further information on materials, ibuprofen crystallization, etoricoxib crystallization, powder X-ray diffraction (pXRD), and lattice plane spacing measurements are available in the Supporting Information.

Safety Statement. No unexpected or unusually high safety hazards were encountered.

■ ASSOCIATED CONTENT

Supporting Information

The Supporting Information is available free of charge at https://pubs.acs.org/doi/10.1021/acscentsci.1c00254.

Titration data, additional TEM and SEM images, and XRD data (PDF)

■ AUTHOR INFORMATION

Corresponding Authors

Helmut Cölfen − *Physical Chemistry, Department of Chemistry, University of Konstanz, 78457 Konstanz, Germany;* orcid.org/0000-0002-1148-0308; Email: helmut.coelfen@uni-konstanz.de

Boris Rybtchinski − *Department of Molecular Chemistry and Materials Science, Weizmann Institute of Science, Rehovot 76100, Israel;* orcid.org/0000-0002-2071-8429; Email: boris.rybtchinski@weizmann.ac.il

Authors

Yael Tsarfati − *Department of Molecular Chemistry and Materials Science, Weizmann Institute of Science, Rehovot 76100, Israel*

Idan Biran − *Department of Molecular Chemistry and Materials Science, Weizmann Institute of Science, Rehovot 76100, Israel*

Eduard Wiedenbeck − *Physical Chemistry, Department of Chemistry, University of Konstanz, 78457 Konstanz, Germany*

Lothar Houben − *Department of Chemical Research Support, Weizmann Institute of Science, Rehovot 76100, Israel;* orcid.org/0000-0003-0200-3611

Complete contact information is available at: https://pubs.acs.org/10.1021/acscentsci.1c00254

Author Contributions

‖Y.T. and I.B. contributed equally.

Notes

The authors declare no competing financial interest.

■ ACKNOWLEDGMENTS

This work was supported by the Israel Science Foundation, Minerva Foundation, and Helen and Martin Kimmel Center for Molecular Design. H.C. and E.W. thank the Deutsche Forschungsgemeinschaft for financial support (Co 194/21-1). We thank Drs. H. Weissman, S. G. Wolf, E. Shimoni, N. Eyal, and I. Kaplan-Ashiri for valuable discussions and assistance with the electron microscopy measurements.

■ REFERENCES

(1) Banfield, J. F. Aggregation-Based Crystal Growth and Microstructure Development in Natural Iron Oxyhydroxide Biomineralization Products. *Science* **2000**, *289*, 751−754.

(2) Hirsch, A.; Palmer, B. A.; Elad, N.; Gur, D.; Weiner, S.; Addadi, L.; Kronik, L.; Leiserowitz, L. Biologically Controlled Morphology and Twinning in Guanine Crystals. *Angew. Chem., Int. Ed.* **2017**, *56*, 9420−9424.

(3) Grotzinger, J. P.; James, N. P. *Carbonate Sedimentation and Diagenesis in the Evolving Precambrian World*; Grotzinger, J. P., James, N. P., Eds.; Society for Sedimentary Geology, 2000.

(4) Yaghi, O. M.; O'Keeffe, M.; Ockwig, N. W.; Chae, H. K.; Eddaoudi, M.; Kim, J. Reticular Synthesis and the Design of New Materials. *Nature* **2003**, *423*, 705−714.

(5) Krieg, E.; Niazov-Elkan, A.; Cohen, E.; Tsarfati, Y.; Rybtchinski, B. Noncovalent Aqua Materials Based on Perylene Diimides. *Acc. Chem. Res.* **2019**, *52*, 2634−2646.

(6) Wolf, T.; Niazov-Elkan, A.; Sui, X.; Weissman, H.; Bronshtein, I.; Raphael, M.; Wagner, H. D.; Rybtchinski, B. Free-Standing Nanocrystalline Materials Assembled from Small Molecules. *J. Am. Chem. Soc.* **2018**, *140*, 4761−4764.

(7) Lu, J.; Litster, J. D.; Nagy, Z. K. Nucleation Studies of Active Pharmaceutical Ingredients in an Air-Segmented Microfluidic Drop-Based Crystallizer. *Cryst. Growth Des.* **2015**, *15*, 3645−3651.

(8) Shekunov, B. Y.; York, P. Crystallization Processes in Pharmaceutical Technology and Drug Delivery Design. *J. Cryst. Growth* **2000**, *211*, 122−136.

(9) Rasenack, N.; Müller, B. W. Ibuprofen Crystals with Optimized Properties. *Int. J. Pharm.* **2002**, *245*, 9−24.

(10) Addadi, L.; Weiner, S. Control and Design Principles in Biological Mineralization. *Angew. Chem., Int. Ed.* **1992**, *31*, 153−169.

(11) De Yoreo, J. J.; Gilbert, P. U. P. A.; Sommerdijk, N. A. J. M.; Penn, R. L.; Whitelam, S.; Joester, D.; Zhang, H.; Rimer, J. D.; Navrotsky, A.; Banfield, J. F.; et al. Crystallization by Particle Attachment in Synthetic, Biogenic, and Geologic Environments. *Science* **2015**, *349*, 349.

(12) Gebauer, D.; Kellermeier, M.; Gale, J. D.; Bergström, L.; Cölfen, H. Pre-Nucleation Clusters as Solute Precursors in Crystallisation. *Chem. Soc. Rev.* **2014**, *43*, 2348−2371.

(13) Gibbs, J. W. On the Equilibrium of Heterogeneous Substance. *Am. J. Sci.* **1878**, *111*, 441−458.

(14) Becker, R.; Döring, W. The Kinetic Treatment of Nuclear Formation in Supersaturated Vapors. *Ann. Phys.* **1935**, *416*, 719−752.

(15) Erdemir, D.; Lee, A. Y.; Myerson, A. S. Nucleation of Crystals from Solution: Classical and Two-Step Models. *Acc. Chem. Res.* **2009**, *42*, 621−629.

(16) Sear, R. P. P. The Non-Classical Nucleation of Crystals: Microscopic Mechanisms and Applications to Molecular Crystals, Ice and Calcium Carbonate. *Int. Mater. Rev.* **2012**, *57*, 328−356.

(17) Davey, R. J.; Schroeder, S. L. M.; ter Horst, J. H. Nucleation of Organic Crystals-A Molecular Perspective. *Angew. Chem., Int. Ed.* **2013**, *52*, 2166−2179.

(18) Sosso, G. C.; Chen, J.; Cox, S. J.; Fitzner, M.; Pedevilla, P.; Zen, A.; Michaelides, A. Crystal Nucleation in Liquids: Open Questions and Future Challenges in Molecular Dynamics Simulations. *Chem. Rev.* **2016**, *116*, 7078−7116.

(19) Gebauer, D.; Völkel, A.; Cölfen, H. Stable Prenucleation Calcium Carbonate Clusters. *Science* **2008**, *322*, 1819−1822.

(20) Gebauer, D.; Wolf, S. E. Designing Solid Materials from Their Solute State: A Shift in Paradigms toward a Holistic Approach in Functional Materials Chemistry. *J. Am. Chem. Soc.* **2019**, *141*, 4490−4504.

(21) Vekilov, P. G. Nucleation. *Cryst. Growth Des.* **2010**, *10*, 5007−5019.

(22) Vekilov, P. G. Two-Step Mechanism for the Nucleation of Crystals from Solution. *J. Cryst. Growth* **2005**, *275*, 65−76.

(23) Wolde, P. R. t.; Frenkel, D. Enhancement of Protein Crystal Nucleation by Critical Density Fluctuations. *Science* **1997**, *277*, 1975−1978.

(24) Vekilov, P. G. Nonclassical Nucleation. *ACS Symp. Ser.* **2020**, *1358*, 19−46.

(25) De Yoreo, J. J. A Perspective on Multistep Pathways of Nucleation. *ACS Symp. Ser.* **2020**, *1358*, 1−17.

(26) Tidhar, Y.; Weissman, H.; Tworowski, D.; Rybtchinski, B. Mechanism of Crystalline Self-Assembly in Aqueous Medium: A Combined Cryo-TEM/Kinetic Study. *Chem. - Eur. J.* **2014**, *20*, 10332−10342.
(27) Shahar, C.; Dutta, S.; Weissman, H.; Shimon, L. J. W.; Ott, H.; Rybtchinski, B. Precrystalline Aggregates Enable Control over Organic Crystallization in Solution. *Angew. Chem., Int. Ed.* **2016**, *55*, 179−182.
(28) Tsarfati, Y.; Rosenne, S.; Weissman, H.; Shimon, L. J. W.; Gur, D.; Palmer, B. A.; Rybtchinski, B. Crystallization of Organic Molecules: Nonclassical Mechanism Revealed by Direct Imaging. *ACS Cent. Sci.* **2018**, *4*, 1031−1036.
(29) Bronshtein, I.; Weissman, H.; Kaplan-Ashiri, I.; Rybtchinski, B. Crystallization of Small Organic Molecules in a Polymer Matrix: Multistep Mechanism Enables Structural Control. *Small* **2019**, *15*, 1902936.
(30) Harano, K.; Homma, T.; Niimi, Y.; Koshino, M.; Suenaga, K.; Leibler, L.; Nakamura, E. Heterogeneous Nucleation of Organic Crystals Mediated by Single-Molecule Templates. *Nat. Mater.* **2012**, *11*, 877−881.
(31) Jiang, Y.; Kellermeier, M.; Gebaue, D.; Lu, Z.; Rosenberg, R.; Moise, A.; Przybylski, M.; Cölfen, H. Growth of Organic Crystals via Attachment and Transformation of Nanoscopic Precursors. *Nat. Commun.* **2017**, *8*, 15933.
(32) Zhang, D.; Zhu, Y.; Liu, L.; Ying, X.; Hsiung, C. E.; Sougrat, R.; Li, K.; Han, Y. Atomic-Resolution Transmission Electron Microscopy of Electron Beam−Sensitive Crystalline Materials. *Science* **2018**, *359*, 675−679.
(33) Almarsson, Ö.; Zaworotko, M. J. Crystal Engineering of the Composition of Pharmaceutical Phases. Do Pharmaceutical Co-Crystals Represent a New Path to Improved Medicines? *Chem. Commun.* **2004**, 1889.
(34) Lee, A. Y.; Erdemir, D.; Myerson, A. S. Crystal Polymorphism in Chemical Process Development. *Annu. Rev. Chem. Biomol. Eng.* **2011**, *2*, 259−280.
(35) Chai, Y.; Wang, L.; Bao, Y.; Teng, R.; Liu, Y.; Xie, C. Investigating the Solvent Effect on Crystal Nucleation of Etoricoxib. *Cryst. Growth Des.* **2019**, *19*, 1660−1667.
(36) Prasad, M. R.; Deb, P. K.; Chandrasekaran, B.; Maheshwari, R. Basics of Crystallization Process Applied in Drug Exploration. In *Dosage Form Design Parameters*; Tekade, R. K., Ed.; Academic Press, 2018; pp 67−103. DOI: 10.1016/B978-0-12-814421-3.00003-8.
(37) Olafson, K. N.; Nguyen, T. Q.; Rimer, J. D.; Vekilov, P. G. Antimalarials Inhibit Hematin Crystallization by Unique Drug−Surface Site Interactions. *Proc. Natl. Acad. Sci. U. S. A.* **2017**, *114*, 7531−7536.
(38) Rimer, J. D.; An, Z.; Zhu, Z.; Lee, M. H.; Goldfarb, D. S.; Wesson, J. A.; Ward, M. D. Crystal Growth Inhibitors for the Prevention of L-Cystine Kidney Stones Through Molecular Design. *Science* **2010**, *330*, 337−341.
(39) Hédoux, A.; Guinet, Y.; Derollez, P.; Dudognon, E.; Correia, N. T. Raman Spectroscopy of Racemic Ibuprofen: Evidence of Molecular Disorder in Phase II. *Int. J. Pharm.* **2011**, *421*, 45−52.
(40) Wiedenbeck, E.; Kovermann, M.; Gebauer, D.; Cölfen, H. Liquid Metastable Precursors of Ibuprofen as Aqueous Nucleation Intermediates. *Angew. Chem., Int. Ed.* **2019**, *58*, 19103−19109.
(41) Warzecha, M.; Verma, L.; Johnston, B. F.; Palmer, J. C.; Florence, A. J.; Vekilov, P. G. Olanzapine Crystal Symmetry Originates in Preformed Centrosymmetric Solute Dimers. *Nat. Chem.* **2020**, *12*, 914−920.
(42) Cookman, J.; Hamilton, V.; Hall, S. R.; Bangert, U. Non-Classical Crystallisation Pathway Directly Observed for a Pharmaceutical Crystal via Liquid Phase Electron Microscopy. *Sci. Rep.* **2020**, *10*, 1−10.
(43) Cookman, J.; Hamilton, V.; Price, L. S.; Hall, S. R.; Bangert, U. Visualising Early-Stage Liquid Phase Organic Crystal Growth via Liquid Cell Electron Microscopy. *Nanoscale* **2020**, *12*, 4636−4644.
(44) Weissman, H.; Rybtchinski, B. Noncovalent Self-Assembly in Aqueous Medium: Mechanistic Insights from Time-Resolved Cryogenic Electron Microscopy. *Curr. Opin. Colloid Interface Sci.* **2012**, *17*, 330−342.
(45) De Yoreo, J. J.; Sommerdijk, N. A. J. M. Investigating Materials Formation with Liquid-Phase and Cryogenic TEM. *Nat. Rev. Mater.* **2016**, *1*, 16035.
(46) Shahar, C.; Baram, J.; Tidhar, Y.; Weissman, H.; Cohen, S. R.; Pinkas, I.; Rybtchinski, B. Self-Assembly of Light-Harvesting Crystalline Nanosheets in Aqueous Media. *ACS Nano* **2013**, *7*, 3547−3556.
(47) Houben, L.; Weissman, H.; Wolf, S. G.; Rybtchinski, B. A Mechanism of Ferritin Crystallization Revealed by Cryo-STEM Tomography. *Nature* **2020**, *579*, 540−543.
(48) Van Driessche, A. E. S. S.; Van Gerven, N.; Bomans, P. H. H. H.; Joosten, R. R. M. M.; Friedrich, H.; Gil-Carton, D.; Sommerdijk, N. A. J. M.; Sleutel, M. Molecular Nucleation Mechanisms and Control Strategies for Crystal Polymorph Selection. *Nature* **2018**, *556*, 89−94.
(49) Patterson, J. P.; Xu, Y.; Moradi, M. A.; Sommerdijk, N. A. J. M.; Friedrich, H. Cryo-TEM as an Advanced Analytical Tool for Materials Chemists. *Acc. Chem. Res.* **2017**, *50*, 1495−1501.
(50) Patrignani, P.; Capone, M. L.; Tacconelli, S. Clinical Pharmacology of Etoricoxib: A Novel Selective COX2 Inhibitor. *Expert Opin. Pharmacother.* **2003**, *4*, 265−284.
(51) Caldwell, J.; Hutt, A. J.; Fournel-Gigleux, S. The Metabolic Chiral Inversion and Dispositional Enantioselectivity of the 2-Arylpropionic Acids and Their Biological Consequences. *Biochem. Pharmacol.* **1988**, *37*, 105−114.
(52) Irvine, J.; Afrose, A.; Islam, N. Formulation and Delivery Strategies of Ibuprofen: Challenges and Opportunities. *Drug Dev. Ind. Pharm.* **2018**, *44*, 173−183.
(53) McConnell, J. F. 2-(4-Isobutylphenyl) Propionic Acid. *Cryst. Struct. Commun.* **1974**, *3*, 73−75.
(54) Hyman, A. A.; Weber, C. A.; Jülicher, F. Liquid-Liquid Phase Separation in Biology. *Annu. Rev. Cell Dev. Biol.* **2014**, *30*, 39−58.
(55) Shankland, N.; Wilson, C. C.; Florence, A. J.; Cox, P. J. Refinement of Ibuprofen at 100K by Single-Crystal Pulsed Neutron Diffraction. *Acta Crystallogr., Sect. C: Cryst. Struct. Commun.* **1997**, *53*, 951−954.
(56) Grobelny, P.; Mukherjee, A.; Desiraju, G. R. Polymorphs and Hydrates of Etoricoxib, a Selective COX-2 Inhibitor. *CrystEngComm* **2012**, *14*, 5785−5794.
(57) De Yoreo, J. J. A Holistic View of Nucleation and Self-Assembly. *MRS Bull.* **2017**, *42*, 525−536.
(58) Tate, M. W.; Purohit, P.; Chamberlain, D.; Nguyen, K. X.; Hovden, R.; Chang, C. S.; Deb, P.; Turgut, E.; Heron, J. T.; Schlom, D. G.; et al. High Dynamic Range Pixel Array Detector for Scanning Transmission Electron Microscopy. *Microsc. Microanal.* **2016**, *22*, 237−249.